Rare Met. (2021) 40(2):489–498
https://doi.org/10.1007/s12598-020-01596-x

RARE METALS
www.editorialmanager.com/rmet

ORIGINAL ARTICLE

Two new pseudo-isomeric nickel (II) metal–organic frameworks with efficient electrocatalytic activity toward methanol oxidation

Shan Liu, Xiao Wang, Hong-Guang Yu, Ya-Pan Wu*, Bo Li, Ya-Qian Lan, Tao Wu, Jian Zhang, Dong-Sheng Li*

Received: 10 June 2020 / Revised: 21 August 2020 / Accepted: 9 September 2020 / Published online: 16 October 2020

Abstract Searching for non-noble metal catalysts with high activities and low price is critical to the commercialization of methanol oxidation in the process of fuel cells. Herein, two new pseudo-isomeric Ni metal–organic frameworks (Ni-MOFs) (CTGU-17/CTGU-18) have been prepared with 1,4-naphthalenedi-carboxylate (H_2NDC), 4,4′-dipyridyl amine (DPA) and $Ni(ClO_4)_2$ under hydrothermal condition. Each phase contains one water molecule, but differs dramatically in its bonding to the framework, resulting in different topological networks with fourfold interpenetrating 4-connected dia net (CTGU-17) and (3,7)-connected net (CTGU-18) and diverse electrocatalytic performance for methanol oxidation reaction (MOR). Remarkably, by combining each MOF with the conductive additive, acetylene black (AB), a composite material, AB&CTGU-18(2:4) was confirmed to have an excellent performance for MOR with a high mass specific peak current of 442.3 $mA \cdot mg^{-1}$. The enhanced electrocatalytic activities and robustness might be attributed to the synergetic effect of acetylene black and the active metal centers of MOFs particles for methanol oxidation. The present work would provide a new insight for the rational design of MOFs-based composites with enhanced methanol oxidation reaction performance.

Keywords Nickel(II); MOFs; Composite materials; Electrocatalysis; Methanol oxidation

1 Introduction

Direct methanol fuel cells (DMFCs) have drawn much attention toward mobile power source applications due to their high energy conversion efficiency, low toxicity, low operating temperature and easy storage and transportation [1–7]. In addition, methanol is safer and cheaper than hydrogen [8]; previous works have demonstrated that Pt group noble metals are recognized to be an efficient electrocatalyst with very high methanol oxidation reaction (MOR) performance [9–15]. However, the use of noble metals has been seriously restricted in DMFCs due to their high cost, low abundance and weak ability of splitting C–C bond [16–18]. Therefore, two key issues should be reasonably addressed: One is the significant reduction in the cost of the catalysts, and the other is substantial enhancement of the anode operation durability and catalytic activity [19, 20].

Up to now, various strategies aimed at designing and tailoring of noble catalysts to achieve further improving better electrocatalytic efficiency, activity and long operational stability. For example, Kang et al. [4] have reported the well-defined Rh nanodendrites with very thin triangular branches as subunits, which exhibited superior mass specific peak current (255.6 $A \cdot g^{-1}$) and long durability (6000 s) in an alkaline medium. Huang et al. [21] have designed and measured MOR performance of Pt-$Ni(OH)_2$-

Electronic supplementary material The online version of this article (https://doi.org/10.1007/s12598-020-01596-x) contains supplementary material, which is available to authorized users.

S. Liu, X. Wang, H.-G. Yu, Y.-P. Wu*, B. Li, Y.-Q. Lan, T. Wu, J. Zhang, D.-S. Li*
College of Materials and Chemical Engineering, Key Laboratory of Inorganic Nonmetallic Crystalline and Energy Conversion Materials, China Three Gorges University, Yichang 443002, China
e-mail: wyapan2008@163.com

D.-S. Li
e-mail: lidongsheng1@126.com

graphene ternary hybrids in alkaline, and these three components have strong mutual interactions to enable remarkable activity (1236 $mA{\cdot}mg^{-1}$ Pt) and unprecedented durability. Although previous works have shown efficient electrocatalytic performance, the use of noble metals cannot be avoided. So, it is of great significance to search high activity and low-cost non-noble electrocatalysts for promoting the practical application of methanol fuel cell.

Recently, metal–organic frameworks (MOFs) have drawn widespread attention on various electrocatalytic processes, due to their controllable morphology, high specific surface area as well as diverse topological networks constructed from different metal centers and specific organic linkers [22–30]. Although nickel plays an important role in the composition of various types of catalysts, Ni-MOFs have hardly been studied in electrocatalyst MOR. We have been committed to exploring nickel(II) MOFs with different structures and research the correlation between their structures and electrocatalytic properties.

In this work, two new pseudo-isomeric Ni-MOFs, [Ni(NDC)(DPA)]·H_2O(CTGU-17), and [Ni_2(NDC)$_2$(DPA) H_2O](CTGU-18)[H_2NDC = 1,4-naphthale-nedicarboxylate, DPA = 4,4′-dipyridyl amine], have successfully designed and synthesized. And they were used for electrocatalytic methanol oxidation reaction. Specially, the integration of Ni-MOFs and acetylene black (AB), AB&CTGU-18 (2:4) hybrid attains efficient electrochemical MOR performance with an impressive mass specific peak current of 442.3 $mA{\cdot}mg^{-1}$ in an alkali medium. The enhanced electro- chemical MOR activity of this composite could be attributed to the possible enhancement of surface area active for the reaction and the improved Ni-MOF conductivity provided by acetylene black incorporated.

2 Experimental

2.1 Materials and methods analysis

All the chemical and reagents were purchased commercially and used directly without further purification. Fourier transform infrared spectroscopy (FTIR) was carried out on a Thermo Electron NEXUS 670 FTIR spectrometer. Powder X-ray diffraction (PXRD) was recorded on a Rigaku Ultima IV diffractometer (Cu Kα radiation, $\lambda = 0.15406$ nm). Thermogravimetric analysis was performed on a Netzsch Model STA 449C microanalyzer in air atmosphere. The N_2 adsorption–desorption isotherms were measured on an automatic surface analyzer (SSA-7300). The morphologies and microstructure were investigated using a field-emission scanning electron microscope (FESEM, JEOLJSM-6700F, Japan) operating at 15 kV and a transmission electron microscopy (TEM, JEOLJEM-2010F) with an accelerating voltage of 200 kV. X-ray photoelectron spectroscopy (XPS) was performed using an ESCALAB 250 with a monochromatic Al Kα X-ray source. Methanol electrooxidation analysis was carried out on a CHI660E at room temperature.

2.2 Experimental details

2.2.1 Synthesis of [Ni(NDC)(DPA)]·H_2O (CTGU-17)

A mixture of H_2NDC (0.1 mmol, 21.6 mg), DPA (8.5 mg), 0.1 $mol{\cdot}L^{-1}$ $Ni(ClO_4)_2$ (2 ml), 0.1 $mol{\cdot}L^{-1}$ NaOH (3 ml) and H_2O (8 ml) was introduced in a 23 ml Teflon-lined stainless steel vessel and then placed in an oven at 140 °C for 3 days. Green block crystals were obtained. Yield: 39% (based on H_2NDC). Elemental analysis (%): cal. for ($C_{22}H_{17}N_3NiO_5$): C 57.18, H 3.71, N 9.10; found: C 57.73, H 3.87, N 9.53. FTIR (cm^{-1}): 3482(w), 3417(w), 3237(w), 3158 (w), 3060 (w), 1600 (s), 1535 (s), 1461 (s), 1423 (s), 1365 (s), 1263 (w), 1209 (m), 1062 (w), 1022 (m), 842 (s), 786 (s), 673 (w), 595 (m), 534 (m) (s represents strong, w represents weak and m represents moderate).

2.2.2 Synthesis of [Ni_2(NDC)$_2$(DPA)(H_2O)](CTGU-18)

The synthesis procedure of CTGU-18 is similar with that of CTGU-17, except that the amounts of DPA, $Ni(ClO_4)_2$ and H_2O were changed to 18 mg, 1 ml, 4 ml, respectively. Yield: 52% (based on H_2NDC). Elemental analysis (%): cal. for ($C_{34}H_{23}$ $N_3Ni_2O_9$):C 55.56, H 3.15, N 5.72; found: C 55.87, H 3.49, N 5.97. FTIR (cm^{-1}): 3470 (w), 3372 (w), 3074 (m), 1596 (s), 1515 (s), 1405 (s), 1353 (s), 1263 (m), 1213 (s), 1022 (m), 905 (w), 902 (w), 817 (s), 782 (s), 665 (w), 592 (m), 536 (w).

2.2.3 Preparation of AB&Ni-MOF hybrid composite

Firstly, the commercial AB powder samples (300 mg) were boiled and washed in deionized H_2O three times and then dried in an 80 °C vacuum oven for 24 h. Secondly, the as-synthesized crystals CTGU-18 (40 mg) were ground to powder and then mixed with AB powder samples (AB) (10, 20, 30 and 40 mg) uniformly to obtain AB&CTGU-18 composites, denoted as AB&CTGU-18 (1:4), AB&CTGU-18(2:4), AB& CTGU-18(3:4) and AB&CTGU-18 (4:4). And the hybrid composites made from CTGU-17 and acetylene black have been obtained via similar strategies as mentioned above. Finally, the composites were confirmed by PXRD, IR, XPS, SEM and TEM measurements.

2.3 X-ray crystallography

The crystal diffraction data for CTGU-17 and CTGU-18 were collected on a XtaLAB diffractometer at 293(2) K

using CuKα radiation (λ = 0.154184 nm). The program CrystalClear was used for integration of diffraction data, and the program SADABS was applied for an empirical absorption correction. The final structure was solved using Olex2 1.2 by direct methods and refined by the full-matrix least-squares technique using SHELXL. All non-H atoms were refined anisotropic thermal parameters. Hydrogen atoms were generated geometrically and further refined isotropically with specific thermal factors. The crystallographic data of CTGU-17 and CTGU-18 were deposited at the Cambridge Crystallographic Data Center (CCDC Nos. 1870144 and 1870145). The crystallographic data and corresponding partial bond lengths and angles for CTGU-17 and CTGU-18 are summarized in Tables 1 [1–12, 22], S1 and S2.

2.4 Procedure of methanol oxidation reaction

Electrochemical measurements were carried out in a three-electrode cell with a solution containing 0.1 mol·L^{-1} KOH and 1.0 mol·L^{-1} CH_3OH. The working electrode is a glassy carbon electrode (ϕ = 3 mm), the reference is Hg/HgO electrode, and the counter electrode is platinum wire. Before testing, the catalyst ink was prepared by mixing 4 mg catalyst with 2 ml H_2O/EtOH (1:1 in volume ratio) and sonicating 30 min. Then, 2 μl suspension was dropped on the electrode and sealed by 1 μl Nafion solution (5 wt%, from Aldrich). The electrode was kept at room temperature and air-dried. The cyclic voltammetry (CV), chronoamperometric ($I - T$) and electrochemical impedance spectroscopy (EIS) were carried out on a CHI660E electrochemical analyzer to assess the properties of catalyst materials. Before electrochemical measurements, the GCE coated with the as-prepared samples was electrochemically activated with a potential cycling window ranging from − 0.2 V to + 1.2 V (vs. SCE) in 0.1 mol·L^{-1} KOH until the as-obtained CV curves tend to coincide.

Table 1 Crystal data and structure refinements for CTGU-17 and CTGU-18

Compounds	CTGU-17	CTGU-18
Formula	$C_{22}H_{17}N_3NiO_5$	$C_{34}H_{23}N_3Ni_2O_9$
Formula weight	462.08	734.95
Temperature/K	293(2)	293(2)
Crystal system	*Orthorhombic*	*Monoclinic*
Space group	*Pbca*	*P*121/*c*1
a/nm	1.3698(4)	0.79731(2)
b/nm	1.5851(2)	1.51426(3)
c/nm	1.7981(3)	2.35320(5)
α/(°)	90	90
β/(°)	90	97.511(2)
γ/(°)	90	90
V/nm^3	3.9042(13)	2.81672(11)
Z	8	4
$D_{cal.}$/(g·cm^{-3})	1.572	1.733
R(int)	0.0360	0.0290
μ/mm^{-1}	1.801	2.250
F (000)	1904.0	1504.0
$R_1[I > 2\sigma(I)]$[a]	0.0375	0.0362
$w_{R_2}[I > 2\sigma(I)]$[b]	0.1036	0.0944
R_1 (all data)	0.0404	0.0386
w_{R_2} (all date)	0.1087	0.0960
GOF on F^2	1.061	1.089
CCDC no.	1,870,144	1,870,145

[a] $R_1 = \sum(|F_o| - |F_c|)/\sum|F_o|$

[b] $w_{R_2} = \left\{\sum\left[w\left(|F_o|^2 - |F_c|^2\right)^2\right]\Big/\sum\left[w\left(|F_o|^2\right)^2\right]\right\}^{1/2}$

3 Results and discussion

3.1 Crystal structure of CTGU-17

Single-crystal X-ray structural analysis shows that CTGU-17 crystallizes the *orthorhombic* system with *Pbca* space group. The asymmetric unit contains one Ni^{2+}, one NDC^{2-}, one neutral DPA ligand and one lattice water molecule. Each Ni^{2+} center is linked to four O atoms (O1, O2, O3#1, O4#1; symmetry codes: #1: 3/2 − *x*, 1/2 + *y*, *z*) from two different H_2NDC ligands and two N (N1, N3#2; symmetry codes: #2: 1/2 − *x*, 1 − *y*, 1/2 + *z*) atoms from two DPA ligands (Fig. S1). The adjacent Ni^{2+} centers are bridged by the carboxylate groups of NDC^{2-} anion with $\mu_2 - \eta^1{:}\eta^1$ mode to generate one 1D zigzag chain structure view along *b* axis. These 1D chains are connected by two DPA molecules to form ultimately single 3D frameworks in the *bc* plane (Fig. 1a). When Ni^{2+} centers could be considered one 4-connected node, the NDC^{2-} and DPA molecules could be simplified as a 2-connected linker; the whole structure of CTGU-17 can be represented as fourfold interpenetrating 4-connected dia networks with point symbol of (6^6) (Fig. 1b).

3.2 Crystal structure of CTGU-18

Although the similar synthetic procedure of CTGU-18 was adopted, one new phase with different structures has been obtained. CTGU-18 crystallizes in monoclinic crystal system with *P*121/*c*1 group. Different with CTGU-17, in each asymmetric unit, there are two crystallographic Ni^{2+}, two NDC^{2-}, one DPA ligand and one coordinated water molecule. Ni1 center adopts six-coordination distorted octahedral geometry, which is ligated by five O atoms (O1,

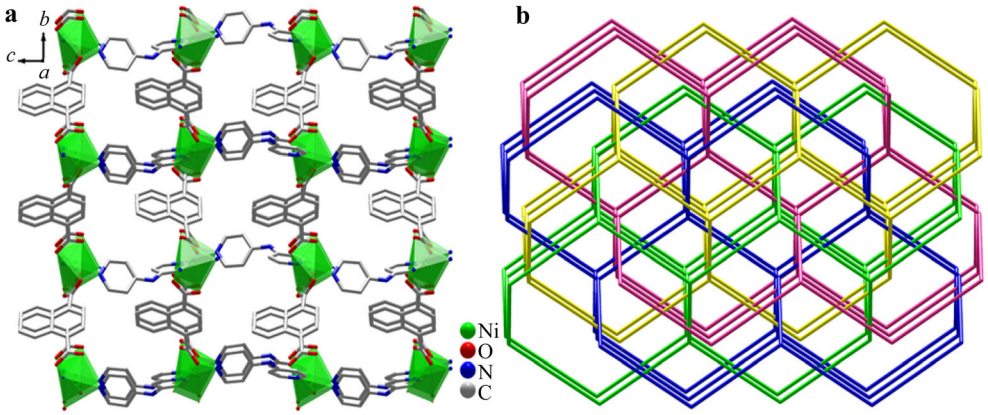

Fig. 1 **a** View of 3D framework viewed along *a* axis; **b** fourfold 4-connected dia networks of CTGU-17

O2, O4#2, O5, O7#3; symmetry codes: #2: $1 - x$, $1 - y$, $1 - z$; #3:$1 - x$, $0.5 + y$, $1.5 - z$) from four different NDC^{2-} ligands and one N atom (N1) from a DPA molecule. And Ni2 center shows similar octahedral geometry, which is bonded with four O atoms (O2, O3#1, O6, O7#3; symmetry codes: #1: $-x$, $1 - y$, $1 - z$; #3:$1 - x$, $0.5 + y$, $1.5 - z$) from four NDC^{2-}, one N atom (N3#4; symmetry code: #4: $-1 + x$, $0.5 - y$, $-0.5 + z$) from a DPA molecule and one O atoms (O9#1) of coordinated water molecule (Fig. S2). The Ni1 and Ni2 centers could be bridged by carboxylate oxygen to generate $\{Ni_2(COO)_4N_2\}$ secondary building unit. Finally, the $\{Ni_2(COO)_4N_2\}$ units are extended by NDC^{2-} and DPA linkers to produce the 3D complicated frameworks along *b* axis (Fig. 2a). Topologically, the NDC^{2-} could be simplified as a 3-connected node, the $\{Ni_2(COO)_4N_2\}$ units are regarded as a 7-connected node, so the overall structure of CTGU-18 has a rare (3,7)-connected $(4^2{\cdot}6)(4^{10}{\cdot}6^{11})$topological net (Fig. 2b). On closer inspection, the amounts of DPA, $Ni(ClO_4)_2$ and H_2O have changed the self-assembly mode of carboxylic acid and metal ions under similar synthetic conditions. And water molecule differs dramatically in its bonding to the framework, which determines the formation of two new phases.

3.3 TGA, FTIR spectra and PXRD results

Thermogravimetric analysis (TGA) curve of CTGU-17 shows a weight loss of 4.1% (cal.: 4.3%) observed from 100 °C to 200 °C, due to the departure of free guest water, and remains stable until 450 °C (Fig. S3a). TGA curve of CTGU-18 shows that the decomposition of the framework begins when the temperature rises above 450 °C (Fig. S3b). Besides, CTGU-17, CTGU-18, AB&CTGU-17 and AB&CTGU-18 were further investigated using FTIR spectroscopy. As shown in Fig. S4, the wide stretching vibration bands in the range of about 3400 cm^{-1} belong to hydroxyl group of water molecules. The peak at about 1530 cm^{-1} could be attributed to the vibrations of C=O. The spectra of AB&Ni-MOF and pure MOF sample are similar, which confirms that the skeletons of two Ni-MOFs are stable before and after composite formation. The main PXRD peaks of the as-prepared CTGU-17 and CTGU-18 crystalline samples are identical with those of single-

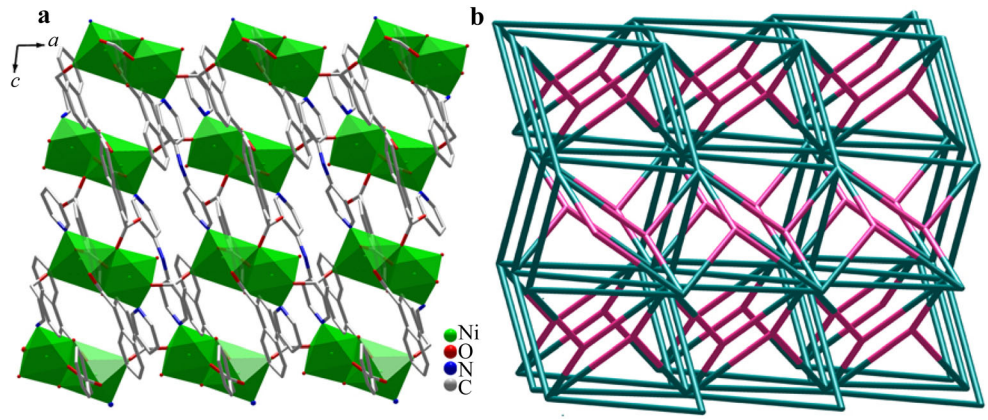

Fig. 2 **a** View of 3D framework viewed along *b* axis of CTGU-18; **b** topological networks with a (3,7-)connected net of CTGU-18

crystal XRD, testifying the phase purity of the samples (Fig. 3). Furthermore, the AB&CTGU-18 and CTGU-18 patterns reveal dispersing diffraction peaks at 25°, which is attributed to the introduction of AB. Meantime, PXRD measurement (Fig. 3) results show that CTGU-17 and CTGU-18 keep high stability immersed in 0.1 mol·L^{-1} KOH for 24 h, also only the surface color of the crystal shows slight changes after immersed in 0.1 mol·L^{-1} KOH (Figs. S5, S6), and the single-crystal data have changed little (Table S3). All these can prove that they should be utilized as stable catalyst in alkaline media.

3.4 Morphological and structural results

Since CTGU-17 and CTGU-18 are pseudo-isomeric, herein, only the morphologic and structural feature of CTGU-18 and its composite was investigated by SEM and TEM. TEM images show that CTGU-18 retains the crystalline block morphology (Fig. S7a). The selected-area electron diffraction (SAED) pattern indicates that as-prepared CTGU-18 sample possesses single-crystal characteristic (Fig. S7b). Also, energy-dispersive spectroscopy (EDS) elemental mapping confirms that the main elements such as Ni, C and O have a uniform distribution in crystalline CTGU-18 (Fig. S7c, d). Figure 4a shows the representative SEM image of AB&CTGU-18 (2:4). AB&CTGU-18 composites have been constructed successfully, and granular acetylene black is uniformly compounded with CTGU-18 crystalline sample. To further demonstrate the composite state of two phases, TEM examination was also performed (Fig. 4b, c). TEM image also reveals that AB&CTGU-18 consists of bulk CTGU-18 which is coated by well-distributed AB. To verify the spatial distribution of the atoms, elemental mapping by EDS was tested, which indicates the homogeneous distributions of nickel, oxygen, carbon and nitrogen in composite material (Fig. 4d). The atom dispersions of Ni, O and N are shown to be concentrated in the MOF samples region, while C atoms are uniformly distributed over the entire material. The results further verify that CTGU-18 is evenly integrated with AB. It is a good strategy to increase conductivity and mechanical properties of MOFs by combining with conductive materials.

Besides, XPS was carried out to understand compositions and oxidation states of pure CTGU-18 and AB&CTGU-18(2:4). Both pure CTGU-18 and composites reveal similar binding energies in XPS spectrum. As shown in Fig. 5a, the XPS survey spectra show the existence of Ni, O, N and C in catalysts, matching with the chemical composition of CTGU-18. However, the intensity of C 1s for CTGU-18 is weaker than that for AB&CTGU-18 (2:4) hybrid. This phenomenon can further indicate that the AB is successfully integrated with CTGU-18. And the Ni $2p_{3/2}$ and Ni $2p_{1/2}$ peaks are centered at binding energies of 855.9 and 873.55 eV, respectively, which are characteristic features of Ni(II) (Fig. 5b). Compared to pure CTGU-18, the AB&CTGU-18(2:4) composite shows a negligible shift of binding energies, indicating that the coordination environment of Ni centers is barely modified after integration of acetylene black. The Brunauer–Emmett–Teller (BET) surface area and BJH pore size distribution were investigated by N_2 adsorption–desorption isotherms measurements at 77 K (Fig. S8). The results demonstrate that AB&CTGU-18(2:4) hybrid sample has a higher BET surface area (13.976 $m^2 \cdot g^{-1}$) than the pure CTGU-18 (8.0478 $m^2 \cdot g^{-1}$). The enhanced surface area may be attributed to the effective conjunction at the interface between CTGU-18 and acetylene black. The high surface

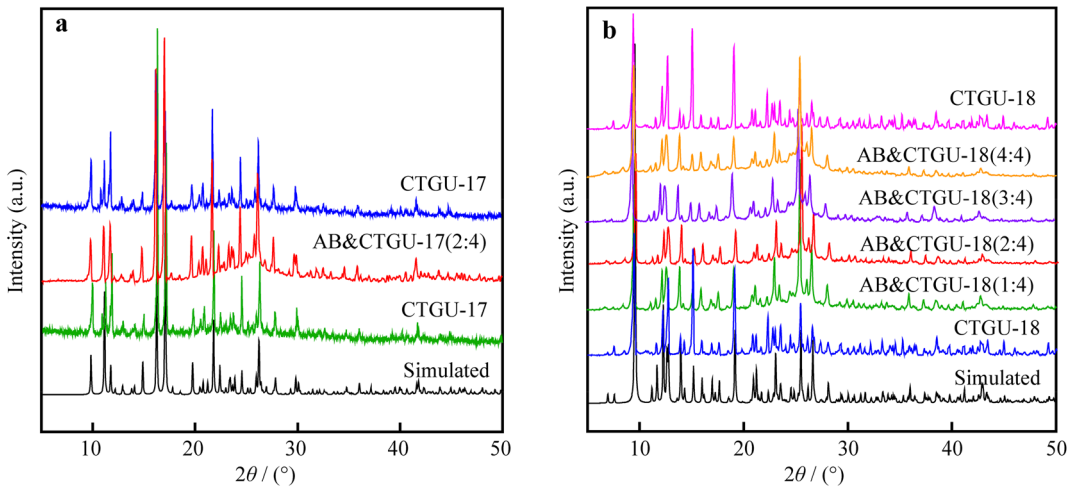

Fig. 3 PXRD patterns of **a** CTGU-17, AB&CTGU-17, CTGU-17 and **b** CTGU-18, AB&CTGU-18, CTGU-18 after immersed in 0.1 mol·L^{-1} KOH for 24 h

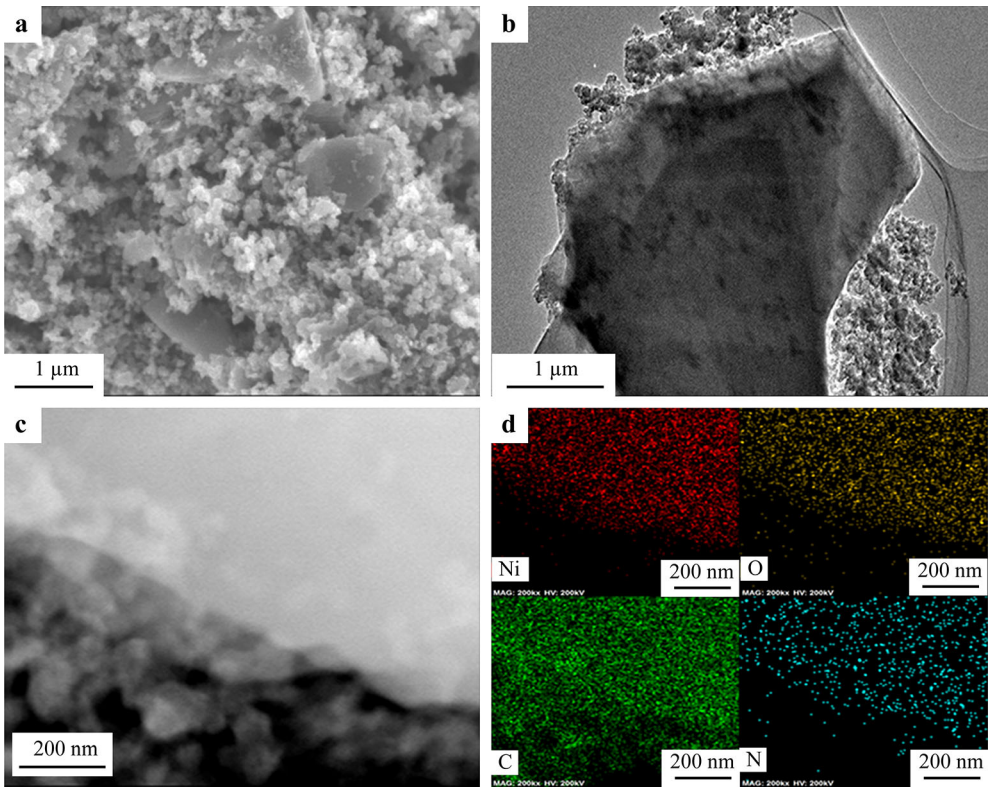

Fig. 4 **a** SEM image, **b, c** TEM images and **d** corresponding EDS mapping images of a part of AB&CTGU-18(2:4) composite, indicating homogeneous distribution of Ni, O, C and N

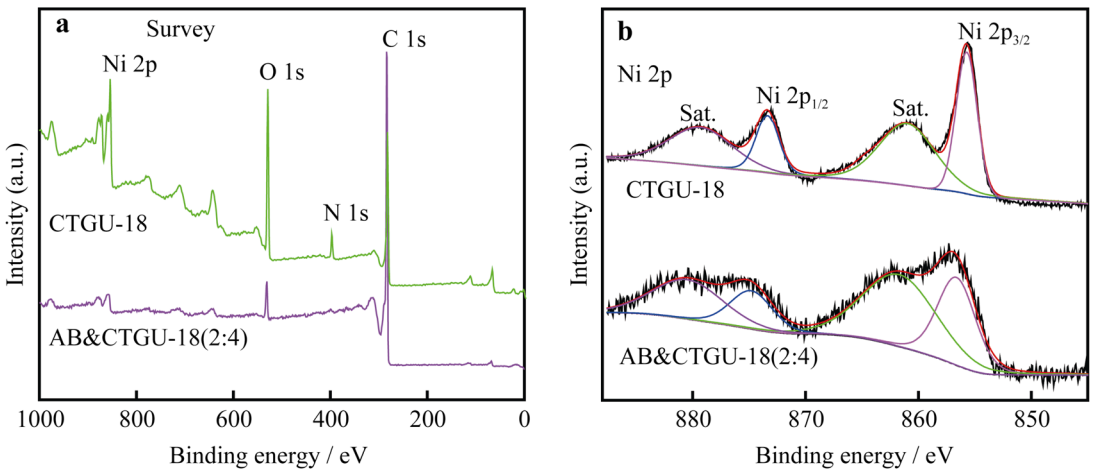

Fig. 5 XPS spectra of CTGU-18 and AB&CTGU-18(2:4) : **a** survey and **b** Ni 2p

area can usually decrease the transportation/diffusion resistance, which can facilitate to accelerate electron transfer and the exposure of active sites during the MOR process.

3.5 Electrocatalytic oxidation of methanol

The as-prepared pure crystalline catalyst loaded glassy carbon electrode was evaluated to study their MOR properties. All of the electrochemical testing was conducted with a typical three-electrode system in a 0.1 $mol \cdot L^{-1}$ KOH aqueous solution containing 1.0 $mol \cdot L^{-1}$ methanol; the potential values were calibrated by RHE. For eliminating the double-layer capacitor effect, all test data were converted into mass activity. The CV curves were expressed to assess the MOR activities of pure MOF and AB&Ni-MOF hybrids. As shown in Fig. 6, obviously, there is no oxidation peak for pure AB-modified

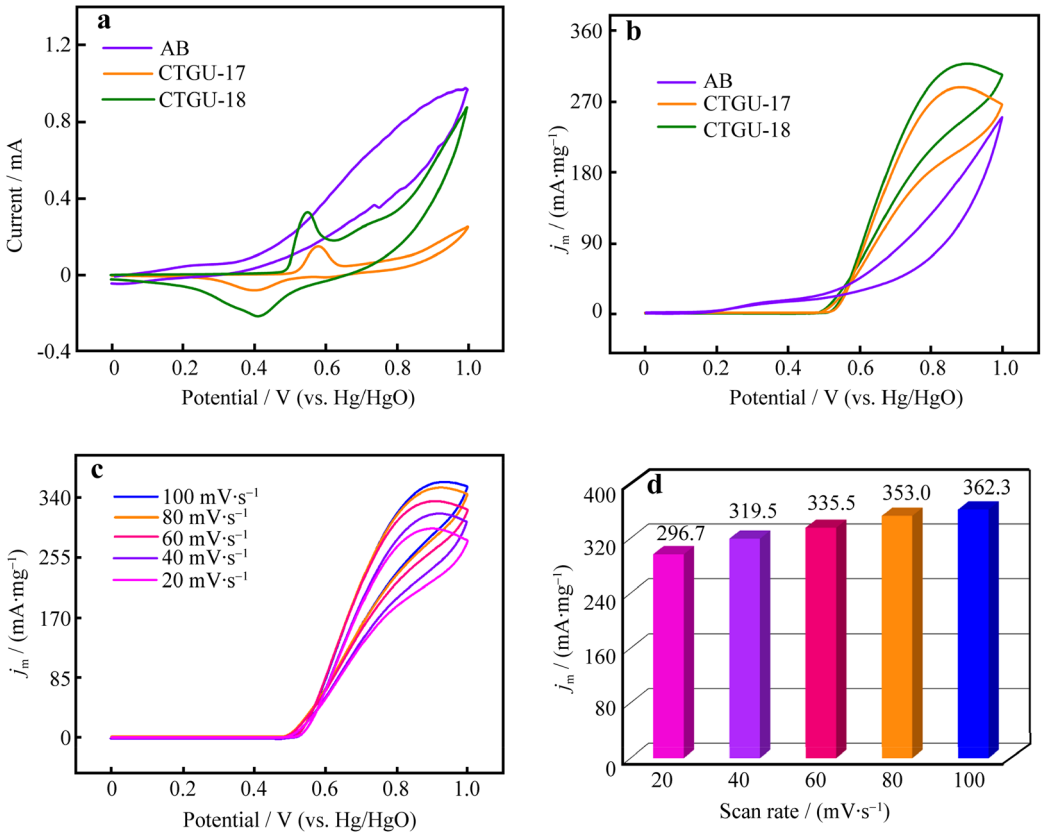

Fig. 6 **a** Cyclic voltammetric response of AB, CTGU-17 and CTGU-18-based electrodes in 0.1 mol·L^{-1} KOH at a scan rate of 50 mV·s^{-1}; **b** MOR curves of two different catalysts operated in 0.1 mol·L^{-1} KOH + 1.0 mol·L^{-1} CH_3OH at a scan rate of 50 mV·s^{-1}; **c** cyclic voltammograms for CTGU-18 at different scan rates; **d** mass-normalized oxidation peak current densities for CTGU-18

electrode in MOR process and also no redox peak in 0.1 mol·L^{-1} KOH electrolyte without methanol, which indicates that AB only plays a role in enhancing conductivity and does not have MOR catalytic activity. By contrast, CTGU-18 exhibits higher MOR activity (318 mA·mg^{-1}) than CTGU-17 (281.25 mA·mg^{-1}) at a scan rate of 50 mV·s^{-1} (Fig. 6b). When the scan rates increase from 20 mV·s^{-1} to 100 mV·s^{-1}, the current density and mass activity of CTGU-18 obviously increase (Fig. 6c, d). Moreover, the peak current densities of CTGU-17 and CTGU-18 increase linearly with the square root of the scan rate for sweep rates from 20 mV·s^{-1} to 100 mV·s^{-1} (Figs. S9, S10). This linear change is attributed to the electrochemical activity of the redox couple over surface of the electrode that expedites speed of reaction.

In order to further clarify the factors contributing to the MOR activity of CTGU-18 crystalline sample, the CV curves for series of hybrid samples made from CTGU-18 and acetylene black were examined in 0.1 mol·L^{-1} KOH in the presence of 1.0 mol·L^{-1} CH_3OH. As shown in Fig. 7a, four electrocatalysts exhibit typical methanol oxidation peak in 0.1 mol·L^{-1} KOH solution at a scan rate of 50 mV·s^{-1}. As expected, the AB&CTGU-18(2:4) hybrid sample obtains the highest MOR activity (442.3 mA·mg^{-1}), which is larger than those of AB&CTGU-18(1:4) (333 mA·mg^{-1}), AB&CTGU-18 (3:4) (398 mA·mg^{-1}) and AB&CTGU-18(4:4) (382.5 mA·mg^{-1}), and 1.39 times higher than that of pure CTGU-18 (318 mA·mg^{-1}) catalyst (Fig. 7b, Table 2). For comparison, the CV for AB&CTGU-17(2:4) was also assessed; it possesses smaller mass activity (409 mA·mg^{-1}) than AB&CTGU-18(2:4) (Fig. S11). The enhanced MOR performance of the as-prepared AB&CTGU-18(2:4) sample indicates relatively lower activation energy for MOR with the integration of available acetylene black. Furthermore, the current densities and the square root of the scan rate in the range from 20 mV·s^{-1} to 100 mV·s^{-1} conform to a linear relationship (Figs. 7c, S12), confirming that the oxidation of methanol is regulated by the diffusion speed.

The durability and long-term activity of pure CTGU-18 and composite electrocatalysts for MOR were studied via chronoamperometry. And the chronoamperometric curves were performed in 0.1 mol·L^{-1} KOH in the presence of 1.0 mol·L^{-1} CH_3OH at a potential step of 0.6 V keeping for 3600 s. As shown in Fig. 7d, the mass activities gradually drop at the very beginning and then

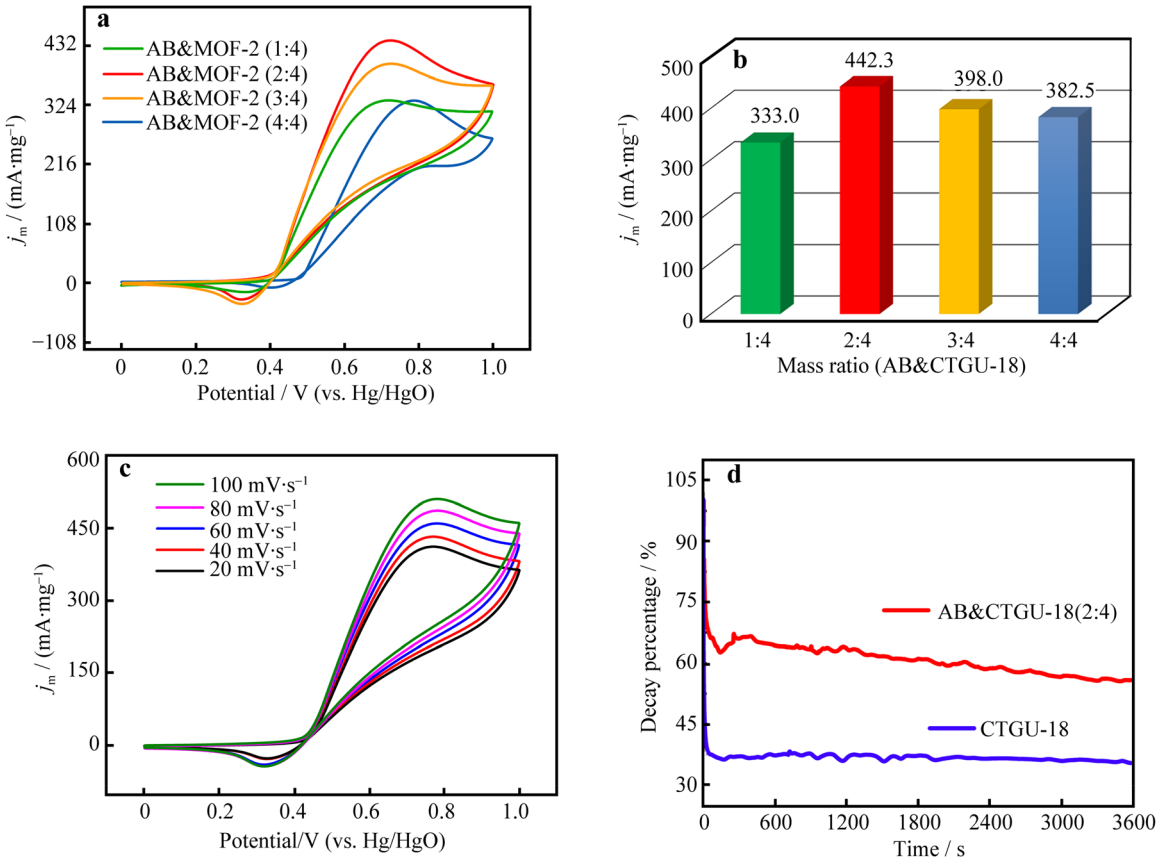

Fig. 7 **a** MOR curves of these four different catalysts operated in 0.1 mol·L^{-1} KOH + 1.0 mol·L^{-1} CH_3OH at a scan rate of 50 mV·s^{-1}; **b** mass-normalized oxidation peak current densities for catalysts; **c** CVs for AB&CTGU-18(2:4) at different scan rates; **d** chronoamperometric curves of CTGU-18 and AB&CTGU-18(2:4) in 0.1 mol·L^{-1} KOH + 1.0 mol·L^{-1} CH_3OH at 0.6 V

slightly reduce for two electrocatalysts. And the slightly decreased current density could be attributed to the poisoning of the catalysts. These curves show that AB&CTGU-18(2:4) (44%) sustains slightly inferior stability than CTGU-18 (65%). Some imperative characterizations such as SEM, TEM, XPS and PXRD were performed to assess the stability of CTGU-17 and CTGU-18 after methanol oxidation reaction. SEM images of CTGU-17 and CTGU-18 indicate that the two catalysts keep their morphology before and after MOR process (Figs. S13, S14). TEM images of CTGU-18 after catalysis maintain the nature of the crystalline material (Fig. S15). PXRD pattern of CTGU-18 (Fig. S15a) recorded after MOR is stable. Also, XPS measurements of CTGU-17 and CTGU-18 before and after MOR were also investigated (Figs. S15b, S16). The Ni 2p spectra have two characteristic peaks with binding energies of around 873 and 856 eV. There are negligible changes in the Ni 2p peaks before and after catalysis, which confirms that the chemical and structural environment is still kept. These results suggest that CTGU-17 and CTGU-18 maintain the original crystalline state after MOR process.

To explore the electrode kinetics of all catalysts, the charge transfer resistances (R_{ct}) was performed. The Nyquist plots of catalysts are shown in Fig. 8. It is found that the R_{ct} of AB&CTGU-18(2:4) (243 Ω) catalyst is smaller than those of other composites such as such as AB&CTGU-18(1:4) (486 Ω), AB&CTGU-18(3:4) (293 Ω), AB&CTGU-18(4:4) (566 Ω) and pure CTGU-18 (743 Ω). The lower R_{ct} value of AB&CTGU-18(2:4) indicates that it delivers highly efficient electron transport and favorable MOR kinetics in the specific electrolyte.

4 Conclusion

In summary, two new pseudo-isomeric nickel(II) MOFs have been prepared and structurally characterized. The electrocatalytic applications for MOR with pure Ni-MOFs and their composites were investigated. The AB&CTGU-18(2:4) hybrid composite attains efficient electrocatalytic MOR performance compared to the pure CTGU-18 electrocatalyst. The enhanced MOR activities could be attributed to the specific active $\{Ni_2(COO)_4N_2\}$ units of Ni-

Table 2 Activity comparison between catalysts in this study and reported catalysts

Catalysts	Activity/(mA·mg^{-1})	Condition/(mol·L^{-1})	Scanning rate/(mV·s^{-1})	Refs.
CTGU-17	281.25	0.1 KOH + 1.0 CH_3OH	50	This work
CTGU-18	318		50	
AB&CTGU-17(2:4)	409		50	
AB&CTGU-18(1:4)	333		50	
AB&CTGU-18(2:4)	442.3		50	
AB&CTGU-18(3:4)	398		50	
AB&CTGU-18(4:4)	382.5		50	
Mesoporous Pt nanoparticles	405	0.5 H_2SO_4 + 0.5 CH_3OH CH_3OH CH_3OH	50	[1]
Hollow dendritic Pt nanocube	242	0.5 H_2SO_4 + 0.5 CH_3OH·CH_3OH	50	[2]
Hollow Pt nanospheres	220	0.5 H_2SO_4 + 1.0 CH_3OH	50	[3]
Pt_3V/C	480	0.1 $HClO_4$ + 1.0 CH_3OH	50	[4]
Hollow Pd@Pt nanoparticles	500	0.5 H_2SO_4 + 1.0 CH_3OH	50	[5]
Ni/NPC-900	449.8	1.0 NaOH +1.0 CH_3OH	50	[6]
CNFs-Ni	400	1.0 KOH +0.5 CH_3OH	50	[7]
Ni@CNTs	966	1.0 KOH + 1.0 CH_3OH	50	[8]
Pt/$Ni(OH)_2$/rGO	1236	1.0 KOH + 1.0 CH_3OH	–	[9]
Pt1Ni1/C	1700	1.0 KOH + 1.0 CH_3OH	50	[10]
AuAg network	15	0.5 KOH + 2.0 CH_3OH	20	[11]
PtRuCu hexapods/C	1350	0.1 $HClO_4$ + 1.0 CH_3OH	50	[12]
CTGU-15	203	0.1 KOH + 1.0 CH_3OH	50	[22]
KB&CTGU-15(1:1)	456	0.1 KOH + 1.0 CH_3OH	50	[22]
KB&CTGU-15(1:2)	527	0.1 KOH + 1.0 CH_3OH	50	[22]
KB&CTGU-15(1:3)	495	0.1 KOH + 1.0 CH_3OH	50	[22]
KB&CTGU-15(1:4)	483	0.1 KOH + 1.0 CH_3OH	50	[22]

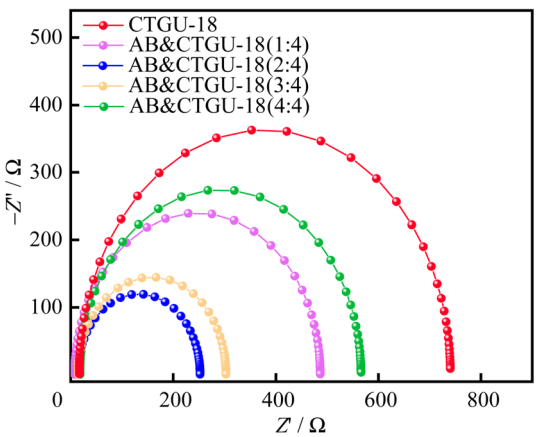

Fig. 8 Nyquist plots of all catalysts measured at 0.6 V (vs. Hg/HgO) in 0.1 mol·L^{-1} KOH + 1.0 mol·L^{-1} CH_3OH, where Z' is real part of impedance and Z'' is imaginary part of impedance

MOF and synergetic effects of acetylene black. These results would confirm that the composite between a Ni-MOF and a conductive additive could be served as an efficient and stable electrocatalyst for methanol oxidation reaction in alkaline media. This work provides a good strategy for replacing noble metal materials with non-noble metal materials as electrocatalysts in future commercial application.

Acknowledgements This work was financially supported by the National Natural Science Foundation of China (Nos. 21971143, 21673127, 21671119, 51572152 and 21805165), the Program of the Ministry of Education of China for Introducing Talents of Discipline to Universities (No. DT20015) and Innovation Team of Young and Middle-aged Research (ITOYMR) in the Higher Education Institutions of Hubei Province (No. T201904).

References

[1] Fu SF, Zhu CZ, Du D, Lin YH. Enhanced electrocatalytic activities of PtCuCoNi three-dimensional nanoporous quaternary alloys for oxygen reduction and methanol oxidation reactions. ACS Appl Mater Interfaces. 2016;8(9):6110.

[2] Xue SF, Deng WT, Yang F, Yang JL, Amiinu IS, He DP, Tang HL, Mu SC. Hexapod PtRuCu nanocrystalline alloy for highly efficient and stable methanol oxidation. ACS Catal. 2018;8(8):7578.

[3] Li R, Ma Z, Zhang F, Meng H, Wang M, Bao XQ, Tang B, Wang X. Facile Cu_3P-C hybrid supported strategy to improve Pt nanoparticle electrocatalytic performance toward methanol, ethanol, glycol and formic acid electro-oxidation. Electrochim Acta. 2016;220:193.
[4] Kang YQ, Li FM, Li SN, Ji PJ, Zeng JH, Jiang JX, Chen Y. Unexpected catalytic activity of rhodium nanodendrites with nanosheet subunits for methanol electro oxidation in an alkaline medium. Nano Res. 2016;9:3893.
[5] Gasteiger HA, Markovic N, Ross PN Jr, Cairns EJ. Methanol electrooxidation on well-characterized platinumruthenium bulk alloys. J Phys Chem. 1993;97(46):12020.
[6] Aricò AS, Srinivasan S, Antonucci V. DMFCs: from fundamental aspects to technology development. Fuel Cells. 2001;1:133.
[7] Zhao X, Yin M, Ma L, Liang L, Liu CP, Liao JH, Lu TH, Xing W. Recent advances in catalysts for direct methanol fuel cells. Energy Environ Sci. 2011;4(8):2736.
[8] Kakati N, Maiti J, Lee SH, Jee SH, Viswanathan B, Yoon YS. Anode catalysts for direct methanol fuel cells in acidic media: do we have any alternative for Pt or Pt-Ru? Chem Rev. 2014;114(24):12397.
[9] Huang H, Ma L, Tiwary CS, Jiang Q, Yin K, Zhou W, Ajayan PM. Worm-shape Pt nanocrystals grown on nitrogen doped low-defect graphene sheets: highly efficient electrocatalysts for methanol oxidation reaction. Small. 2017;13(10):1603013.
[10] Huang M, Zhang J, Wu C, Guan L. Pt nanoparticles densely coated on SnO_2-covered multiwalled carbon nanotubes with excellent electrocatalytic activity and stability for methanol oxidation. ACS Appl Mater Interfaces. 2017;9(32):26921.
[11] Munjewar SS, Thombre SB, Mallick RK. Approaches to overcome the barrier issues of passive direct methanol fuel cell-review. Renew Sustain Energy Rev. 2017;67:1087.
[12] Xia BY, Wu HB, Wang X, Lou XW. One-pot synthesis of cubic $PtCu_3$ nanocages with enhanced electrocatalytic activity for the methanol oxidation reaction. J Am Chem Soc. 2012;134(34):13934.
[13] Meng C, Ling T, Ma TY, Wang H, Hu Z, Zhou Y, Mao J, Du XW, Jaroniec M, Qiao SZ. Atomically and electronically coupled Pt and CoO hybrid nanocatalysts for enhanced electrocatalytic performance. Adv Mater. 2017;29(9):1604607.
[14] Yang PP, Yuan XL, Hu HC, Liu YL, Zheng HW, Yang D, Chen L, Cao MH, Xu Y, Min YL, Li YG, Zhang Q. Solvothermal synthesis of alloyed PtNi colloidal nanocrystal clusters (CNCs) with enhanced catalytic activity for methanol oxidation. Adv Funct Mater. 2018;28(1):1704774.
[15] Zhang T, Bai Y, Sun YQ, Hang LF, Li XY, Liu DL, Lyu XG, Li CC, Cai WP, Li Y. Laser-irradiation induced synthesis of spongy AuAgPt alloy nanospheres with high-index facets, rich grain boundaries and subtle lattice distortion for enhanced electrocatalytic activity. J Mater Chem A. 2018;6(28):13735.
[16] Zeng ZP, Xiao FX, Phan H, Chen SF, Yu ZZ, Wang R, Nguyen T, Tan TTY. Unraveling the cooperative synergy of zero-dimensional graphene quantum dots and metal nanocrystals enabled by layer-by-layer assembly. J Mater Chem A. 2018;6(4):1700.
[17] Yu YC, Xin HL, Hovden R, Wang DL, Rus ED, Mundy JA, Muller D, Abruña HD. Three-dimensional tracking and visualization of hundreds of Pt-Co fuel cell nanocatalysts during electrochemical aging. Nano Lett. 2012;12(9):4417.
[18] Chen C, Kang YL, Huo ZY, Zhu ZW, Huang WY, Xin HL, Snyder JD, Li DG, Herron JA, Mavrikakis M, Chi MF, More KL, Li YD, Markovic NM, Somorjai GA, Yang PD, Stamenkovic VR. Highly crystalline multimetallic nanoframes with three-dimensional electrocatalytic surfaces. Science. 2014;6177(343):1339.
[19] Chen L, Du R, Zhu JH, Mao YY, Xue C, Zhang N, Hou YL, Zhang J, Tao Y. Three-dimensional nitrogen-doped graphene nanoribbons aerogel as a highly efficient catalyst for the oxygen reduction reaction. Small. 2015;11(12):1423.
[20] Guo SJ, Zhang S, Sun SH. Tuning nanoparticle catalysis for the oxygen reduction reaction. Angew Chem Int Ed. 2013;52(33):8526.
[21] Huang WJ, Wang HT, Zhou JG, Wang J, Duchesne PN, Muir D, Zhang P, Han N, Zhao FP, Zeng M, Zhong J, Jin CH, Li YG, Lee ST, Dai HJ. Highly active and durable methanol oxidation electrocatalyst based on the synergy of platinum-nickel hydroxide-graphene. Nat Commun. 2015;6:10035.
[22] Wu YP, Tian JW, Liu S, Li B, Zhao J, Ma LF, Li DS, Lan YQ, Bu X. Bi-microporous metal-organic frameworks with cubane $[M_4(OH)_4]$(M = Ni, Co) clusters and pore-space partition for electrocatalytic methanol oxidation reaction. Angew Chem Int Ed. 2019;58(35):12185.
[23] Singh BK, Lee S, Na K. An overview on metal-related catalysts: metal oxides, nanoporous metals and supported metal nanoparticles on metal organic frameworks and zeolites. Rare Met. 2020;39(7):751.
[24] Huang D, Wu X, Tian J, Wang X, Zhou Z, Li D. Assembling of a novel 3D Ag(I)-MOFs with mixed ligands tactics: syntheses, crystal structure and catalytic degradation of nitrophenol. Chin Chem Lett. 2018;19(7):845.
[25] Wu YP, Zhou W, Zhao J, Dong WW, Lan YQ, Li DS, Sun CH, Bu XH. Surfactant-assisted phase-selective synthesis of new cobalt MOFs and their efficient electrocatalytic hydrogen evolution reaction. Angew Chem Int Ed. 2017;56(42):13001.
[26] Wang X, Zhou W, Wu YP, Tian JW, Wang XK, Huang DD, Zhao J, Li DS. Two facile routes to an AB&Cu-MOF composite with improved hydrogen evolution reaction. J. Alloys. Compd. 2018;753:228.
[27] Shi YK, Wang W, Liu YJ, Liu JJ, Wang L, Guo Y. Catalytic combustion performance of Co_3O_4 derived from metal-organic framework. Chin J Rare Met. 2019. http://kns.cnki.net/kcms/detail/11.2111.TF.20190923.1552.011.html.
[28] Zhou W, Wu YP, Wang X, Tian JW, Huang DD, Zhao J, Lan YQ, Li DS. Improved conductivity of a new Co(II)-MOF by assembled acetylene black for efficient hydrogen evolution reaction. Cryst Eng Comm. 2018;20(33):4804.
[29] Cheng WZ, Liang JL, Yin HB, Wang YJ, Yan WF, Zhang JN. Bifunctional iron-phtalocyanine metal–organic framework catalyst for ORR, OER and rechargeable zinc–air battery. Rare Met. 2020;39(7):815.
[30] Lu XF, Liao PQ, Wang JW, Wu JX, Chen XW, He CT, Zhang JP, Li GR, Chen XM. An alkaline-stable, metal hydroxide mimicking metal-organic framework for efficient electrocatalytic oxygen evolution. J Am Chem Soc. 2016;138(27):8336.